AIAA AVIATION 2016
13 - 17 Jun 2016, Washington, DC

AIAA-2016-3348

Optical Measurements of Transitional Events in a Mach-6 Laminar Boundary Layer

Stanislav Gordeyev[1] and Thomas J. Juliano[2],
Department of Aerospace and Mechanical Engineering,
University of Notre Dame, Notre Dame, IN 46556

Results of aero-optical measurements of the naturally occurring transitional structures, turbulent spots, and second-mode wave-packet structures in the hypersonic laminar boundary layer are presented. Optical spectra of turbulent spots were similar to spectra for the fully turbulent boundary layers and the average thickness of the boundary layer during the turbulent spot was approximately 50% of the fully turbulent boundary layer. The convective speed of the leading edge of the spot was measured as 0.95 of the freestream speed, while the trailing edge moves at 0.7 of the freestream speed. The dominant frequency of the wave-packet structures was about 70 kHz, consistent with the theoretically predicted second-mode frequency; the average convective speed of the packets was measured as 0.88 of the freestream speed. Using the frozen-field hypothesis, the wavefronts were stitched together to reveal streamwise/spanwise topology of the packets. The packets were found to be fairly narrow, about 2-3δ in the spanwise direction, extending for 30-60δ in the streamwise direction, and having an unusual "reverse-bow" topology.

I. Introduction

AERO-OPTICAL effects [1,2] are the result of the dependence of the index-of-refraction, *n*, on the density in air, ρ, via the Gladstone-Dale constant, K_{GD} (which is approximately 2.27×10^{-4} m^3/kg in air for visible wavelengths of light), $n(\bar{x},t)-1=K_{GD}\rho(\bar{x},t)$. Light passing through regions of unsteady turbulent flow is distorted by the spatially- and temporally-fluctuating density fields present along the optical path length. The effect of turbulent density fluctuations on the propagation of light can be quantified by defining the Optical Path Difference (OPD) as the average-removed integral of the index-of-refraction of a medium along the physical length traversed by a ray of light,

$$OPD(x,y,t)=\int n'(x,y,z,t)dz = K_{GD}\int \rho'(x,y,z,t)dz$$

where primes denote mean-removed fluctuations and *z* is the direction of beam propagation.

The state of a hypersonic boundary layer --- whether it is laminar, transitional, or turbulent --- is an important factor in the design of hypersonic vehicles due to its effect on surface heating, skin friction, separation, aero-optical distortion, and other boundary-layer properties [3]. Thus, the boundary-layer state's aero-optical impact can be exploited as a means to study the boundary layer. In this experiment, a Shack-Hartmann wavefront sensor, which non-intrusively measures density fluctuations, was used to investigate various transitional events, namely short turbulent spots and second-mode transitional structures, in a laminar hypersonic boundary layer at high Reynolds numbers. These structures were studied before using primarily wall-mounted sensors [4,5,6]. This non-intrusive optical technique offers several advantages. The interrogation region can be smaller than that of a typical pressure transducer and multiple optical sensors can be clustered more tightly

---

[1] Research Associate Professor, Department of Mechanical and Aerospace Engineering, Hessert Laboratory for Aerospace Research, Notre Dame, IN 46556, AIAA Associate Fellow.

[2] Assistant Professor, Department of Mechanical and Aerospace Engineering, Hessert Laboratory for Aerospace Research, Notre Dame, IN 46556, AIAA Senior Member.

than physical transducers. Additionally, the boundary-layer density fluctuation spectrum can be assessed simultaneously with the wall shear stress or unsteady pressure. One wavefront sensor can replace several individual transducers for the measurement of convective speeds and directions of density fluctuations thus *a priori* knowledge of the disturbances to optimize sensor layout is avoided. Also, the non-intrusive nature of aero-optical measurements makes them very attractive to study transitional hypersonic boundary layers, which generally are very sensitive to any surface defects [7].

While the aero-optics of turbulent boundary layers has been extensively studied in recent years [2, 8 and references therein], including experimental measurements [9,10,11] and numerical simulations [12,13,14] in high supersonic and hypersonic turbulent boundary layers, aero-optical measurements of transitional events in laminar boundary layers at high speeds are limited and many important questions about the details of the dynamics and topology of underlying structures remain unanswered. The highly spatially and temporally resolved optical data yielded by the Shack-Hartmann wavefront sensor can provide valuable quantification of the amplification and propagation of disturbances within a transitional boundary layer.

II. Experimental Set-Up

The data presented herein were collected in the Boeing/AFOSR Mach-6 Quiet Tunnel at Purdue University (BAM6QT). The Ludwieg tube configuration is shown in Figure 1. While running quietly, the noise level is less than 0.05%, and it increases to about 3% when noisy [15].

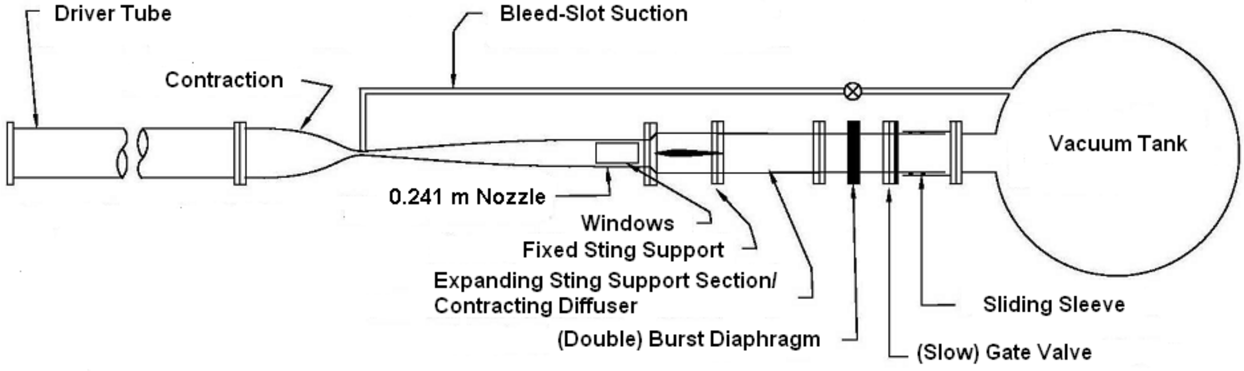

Figure 1: BAM6QT schematic.

The BAM6QT employs many features to maintain a laminar nozzle-wall boundary layer, thereby achieving quiet flow. The valve in the bleed-slot suction plumbing can be set to open or remain closed during a run, permitting the user to control whether the nozzle-wall boundary layer is laminar (for quiet flow) or turbulent (noisy flow). A more comprehensive discussion of the components of the BAM6QT is contained in [5].

The air is heated to a nominal stagnation temperature of 433 K, corresponding to a static temperature of 53 K when expanded to Mach 6. The freestream Mach number in the test section is 6.0 under quiet flow and varies slightly with stagnation pressure. Thicker, turbulent nozzle-wall boundary layers reduce the freestream Mach number to 5.8 when running with conventional noise levels.

The BAM6QT test section accommodates several interchangeable inserts [16]. For these tests, two windows with 4-cm viewable diameters were installed at an axial station 1.924 m from the nozzle throat in the forward ports of the 75 x250 mm window inserts [17].

Several runs with different stagnations pressures were performed, see Table 1. All runs were performed under the quite tunnel regime. For the range of stagnation temperatures, the freestream speed was approximately 870 m/s. Runs B2, B4, B6 and B8 contain two independent runs under the same conditions to increase the sampling time. Using laminar boundary-layer simulations, reported in [18], for the range of stagnation pressures between 50 and 150 psi, the laminar boundary thickness was extrapolated to be 5.6 mm for all runs. Reynolds number per unit length was 13.5M/m, giving $Re_\delta = 75{,}800$.

Table 1. Initial flow parameters and test conditions.

Run #	P_0 (psi)	T_0 (C)	Aperture Size (mm)	Aperture location	Sampling Frequency (Hz)
Run A8	175	151	9.5 x 1.2	10 mm above centerline	1,000,000
Run A11	170	151	9.5 x 1.2	14 mm above centerline	1,000,000
Run B2	175	159	35 mm diameter	centerline	30,000
Run B4	174	155	11.4 x 5.7	centerline	531,645
Run B6	174	153	11.5 x 5.7	10 mm above centerline	531,645
Run B8	175	152	22.9 x 11.5	centerline	250,000

All measurements were performed using a high-speed Shack-Hartmann WaveFront Sensor (WFS); a schematic of the experimental set-up is shown in Figure 2. The laser beam was expanded to 40-mm diameter and passed perpendicularly through two flat windows mounted in the test section. When passed through the test section, the laser beam encountered two hypersonic boundary layers, one on each side of the test section. After reflecting from the return mirror, the beam traversed back to the optical table exactly the same way it came, the so-called double-pass experiment. The returning beam was split off using a cube beam splitter, contracted to a 12.5-mm diameter using a contracting telescope and finally sent to a Phantom v1611 high-speed digital camera. The camera had a 38-mm focal length, 70x60 lenslet with 0.3-mm-pitch, attached to it. After passing through the lenslet array, the beam was split into subaperture beams and focused on the camera sensor, creating a series of dots. To collect the wavefronts over the entire aperture with the spatial resolution of 37 subapertures in each direction, the sampling rate was reduced to 30,000 Hz in Run B2. To achieve the high sampling rate of 1,000,000 fps, only a small, 128x16-pixel portion of the image, corresponding to a single line of 11 subapertures, was sampled for 4 seconds for Runs A8 and A11 (Figure 3). Finally, wavefronts were collected at 531,645 Hz for Runs B4 and B6 and at 250,000 for Run B8 with proportionally-reduced aperture sizes.

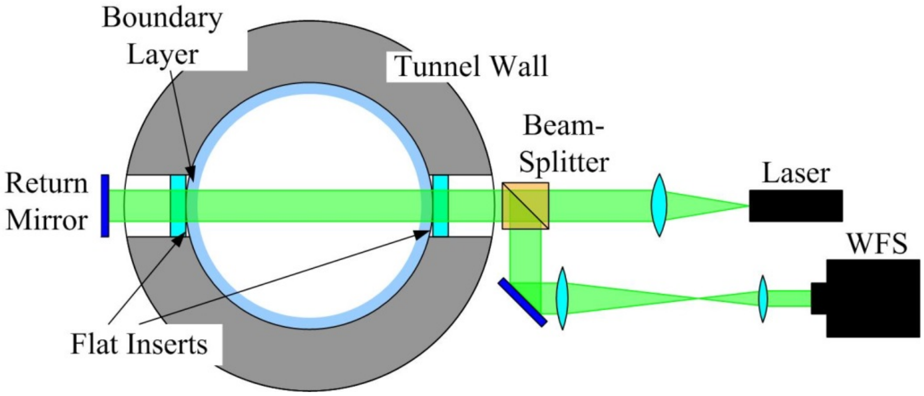

Figure 2. Schematics of BL experimental set-up.

Simultaneously with aero-optical measurements, local heat transfer information was collected by Senflex hot film sensor mounted at the bottom of on the nozzle wall 190 mm downstream of the beam location. It was controlled by a Bruhn 6 constant-temperature anemometer and sampled at 1,000 kHz for the duration of each run. These sensors are uncalibrated and customarily used to verify qualitatively the condition of the nozzle-wall boundary layer (laminar, turbulent, or separated). A Kulite pressure transducer flush-mounted to the contraction inlet provided the stagnation pressure during the run. A Tektronix digital oscilloscope in Hi-Res mode was used to record the output voltages of the hot films and Kulite.

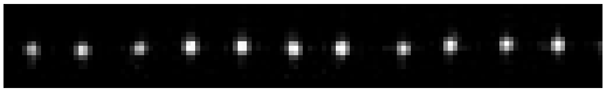
Figure 3. 16 x 128 wavefront image.

Several runs were performed with the aperture center aligned with the centerline of both inserts. In this case, when only a streamwise line of the subapertures was sampled during Run B8, there were no step between the flat inserts and the contoured tunnel wall upstream measurement location. For Runs A8 and B6, the sampling area was shifted 10 mm up, so a small backward-facing step of approximately 0.4 mm was present upstream of the measurement location, potentially perturbing the boundary layer over the flat inserts. Finally, the sampling area was shifted up by 14 mm during Run A11, resulted in the backward-facing step of 0.8 mm upstream of the measurement area.

III. Data Analysis

For each run, temporal evolutions of the dots' centroids were extracted using in-house software and converted into time-series deflection angles at different subapertures. These measurements are essentially equivalent to measurements using a multi-beam Malley probe [8,11]. The deflection angle time series were used to identify the transitional events using various thresholding techniques, described later in the paper. The deflection angles are local gradients of the wavefront, so they were used to reconstruct the spatial-temporal 2-D wavefront sequences over the aperture using the Southwell method [19].

For runs with large apertures, Runs B2, B4, B6, instantaneous tip/tilt and piston modes were removed from each wavefront. To eliminate the corrupting effect of the tunnel vibrations, a moving averaging filter with the duration of 0.2 ms was also applied to the wavefront sequences.

To compute speeds of aero-optical distortions for Runs A8, A11, B4 and B6, the deflection angles at different points over the aperture were cross-correlated at various time delays. Determining a local maximum in the correlation,

$$C(\Delta x,\tau)=\left\langle \int \theta(x,t)\theta(x+\Delta x,t+\tau)dx \right\rangle, \quad \max(C)\to \tau(\Delta x),$$

where angled brackets denote ensemble averaging over all possible pairs of points with the fixed streamwise separation Δx, gives measurements of the convective speed as a slope between Δx and τ.

For Run B8, a similar technique was used, but this time, a correlation between two sequential frames was computed, $C(\Delta x,\Delta t;T)=\int \theta(x,T)\theta(x+\Delta x,T+\Delta t)dx, \quad \max(C)\to \Delta x$, where $\Delta t = 1/f_{\mathrm{samp}}$ is a time interval between two frames, and the convective speed at the time T was computed as $U_C(T) = \Delta x/\Delta t$.

IV. Results

Analysis of the previously-collected aero-optical data [20] and surface unsteady pressures [4] in the tunnel had shown that the boundary layer is fully laminar for stagnation pressures below 140 psi. Above this pressure, the freestream Reynolds number becomes large enough to cause intermittent transitional events in the laminar boundary layer [4]. Example of the time series of the deflection angle is presented in Figure 4, top. For most of the time the deflection angle exhibits only low-frequency, tunnel-vibration-related decaying oscillations, indicating that the boundary layer was laminar during the most of the run. However, at several instances, the time series exhibit intermittent, short-lived increases in the deflection angle amplitude. A close inspection of the time series had revealed the presence of two types of the transitional events. The first one, shown in Figure 4, bottom left, indicated a presence of a short turbulent spot. The second one, shown in Figure 4, bottom right, appeared to an even shorter-lived single-frequency wave-packet event, which was identified to be a transitional second-mode-instability wave packet.

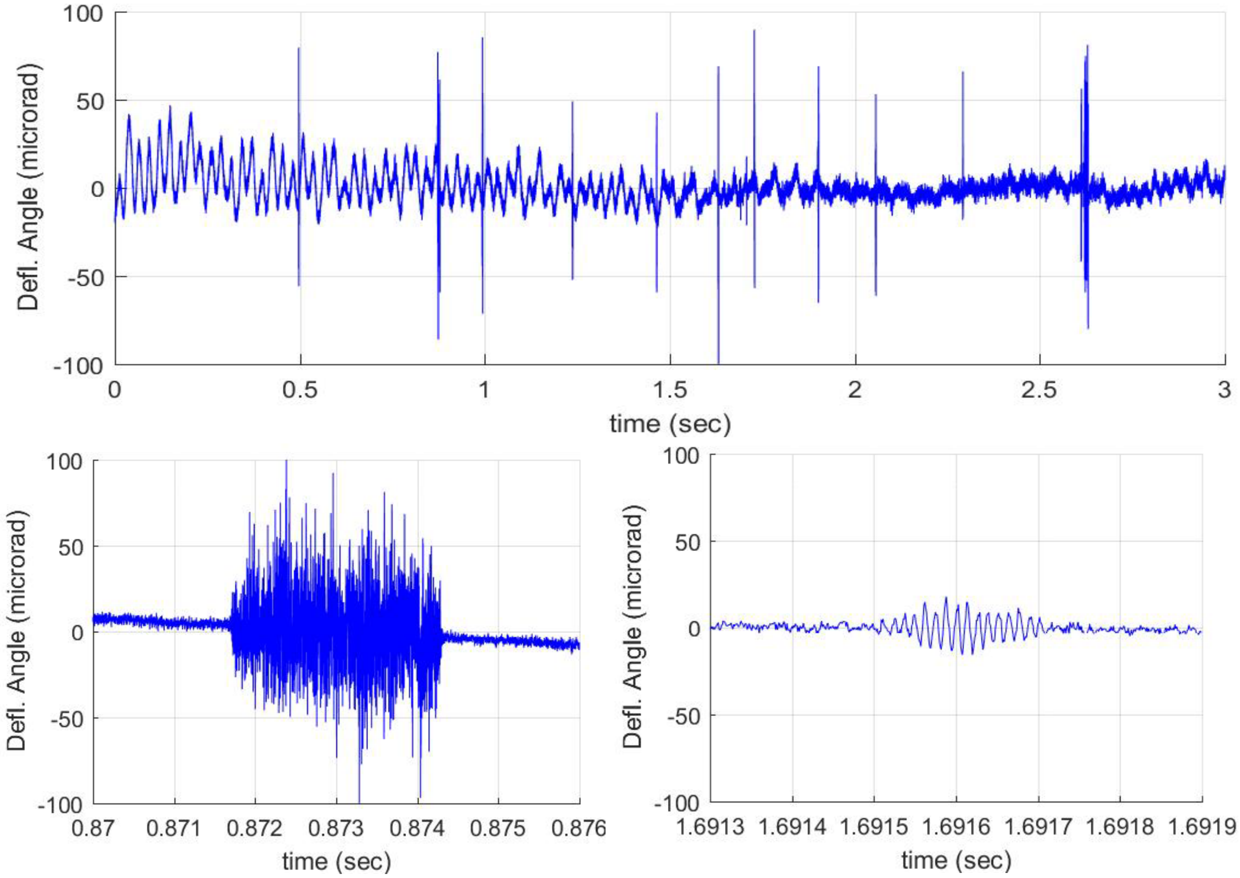

Figure 4. Long time series of the deflection angle for Run A8 (top), expanded time series showing a localized broad-band increase, associated with the turbulent spot (bottom left) and a single-frequency event, corresponding to the second mode (bottom right).

Turbulent spots

Turbulent spots or bursts, one of them shown in Figure 4, bottom left, are characterized by broad-spectrum fluctuations typical of a turbulent boundary layer. This flow feature is well-known and was observed and documented in this tunnel by other researches [4,5,6]. To study the statistics of the turbulent spots, time periods with either large spatial (Run B2) or temporal (Runs, A8, A11, B4, B6, B8) wavefront fluctuations were extracted from wavefront sequences; total of 373 turbulent-spot events were extracted from all runs. For each event, the event duration was determined and the probability distribution was computed, see Figure 5. The average turbulent-spot duration was found to be about 1.42 ms, with the shortest event of 1.15 ms and the longest one of 1.8 ms; 75% of the events were found to be between 1.3 and 1.5 ms. Later in this paper it will be shown that this duration is consistent with the notion that the turbulent spot originates in the nozzle throat, as suggested in [4].

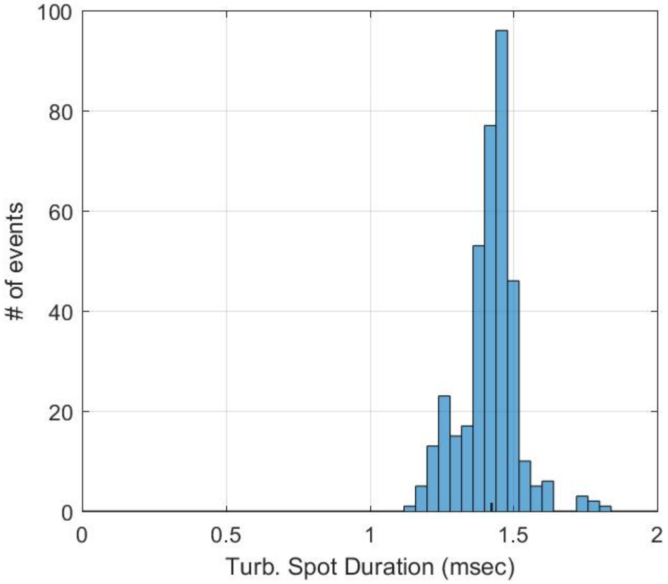

Figure 5. Statistics of the turbulent spot duration at the measurement station.

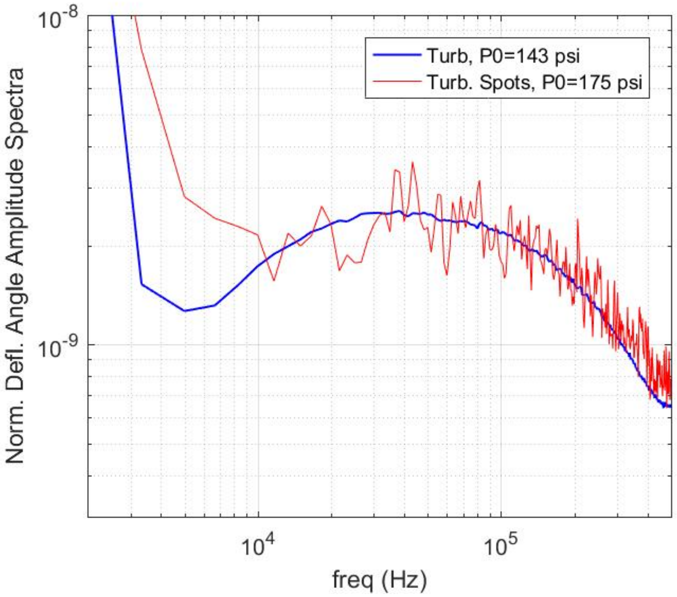

Figure 6. Comparison between the deflection angle spectra for the fully turbulent boundary layer [20] and during the turbulent spot. Both spectra are normalized by the freestream density.

Time series during the turbulent spots for Runs A8 and A11 were used to calculate the deflection angle spectrum, which is presented in Figure 6 (red line). Comparison with the fully turbulent boundary-layer spectrum [20], represented by a black line in Figure 6, indicated that the boundary layer during the turbulent spots is quite similar to a fully turbulent boundary layer. The turbulent-spot spectrum has slightly larger optical energy in the high frequencies above 200 kHz and possibly lower energy between 20 and 40 kHz; however using less than 400 events precludes having a well-converged spectrum and additional measurements are required to obtain more events and to improve the accuracy of the spectrum calculation.

The comparison of the deflection angle time series with the hot film sensor, mounted on the bottom of the tunnel wall 0.19 m downstream the measurements station, with several examples shown in Figure 7, revealed that the turbulent boundary layer was present simultaneously on the bottom and both sides of the tunnel. It indicates that the turbulent spot engulfs the full tunnel circumference at the measurement location and consistent with the similar conclusion drawn in [4].

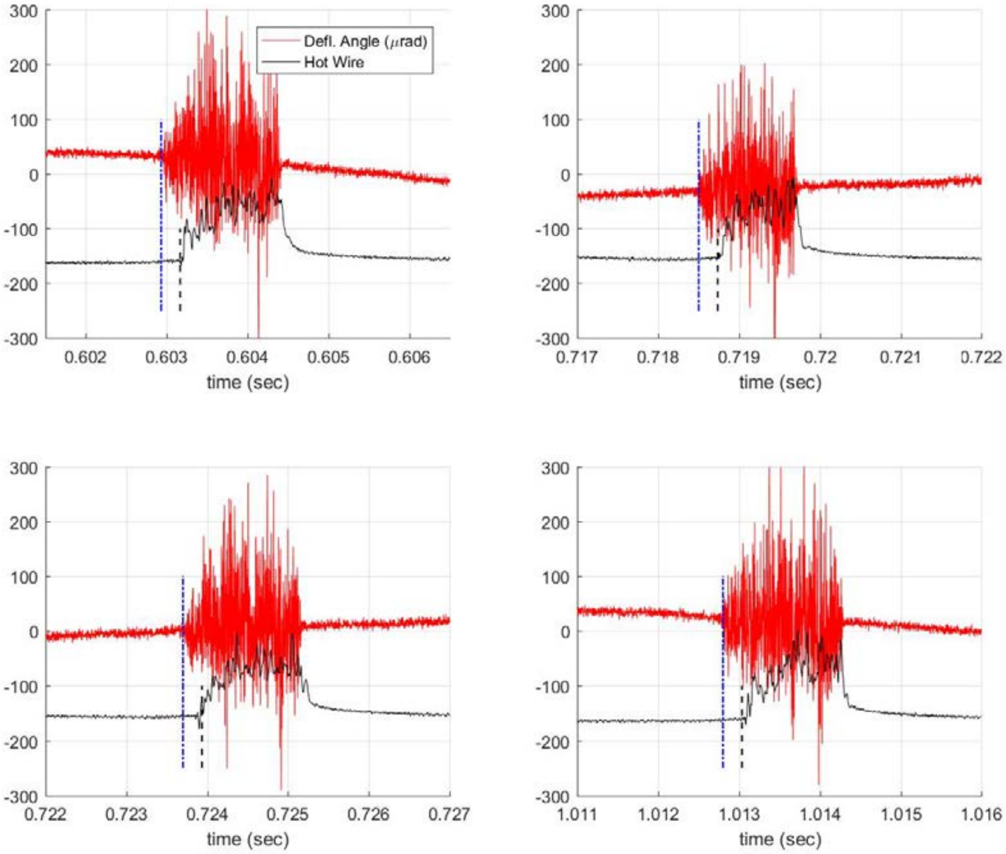

Figure 7. Four examples of simultaneous optical (deflection angle) and the hot-film signals, indicating that the turbulent spot was simultaneously present over the optical measurement station and at the bottom of the tunnel. Dashed-dotted lines indicate the beginnings of each turbulent spot in the deflection-angle time series and dashed lines are delayed from the beginnings of the turbulent spot by 0.235 ms.

In [4] the convective speeds of both the leading and the trailing edges of the turbulent spots were directly measured using a series of unsteady pressure sensors placed between 2.2 m and 2.8 m from the nozzle throat. Note that the leading and trailing edges of the spot are the down- and upstream edges, respectively. The leading-edge convective speed was found to be approximately $0.93U_\infty$. Using this convective speed, a time delay for the leading edge of turbulent spot to travel the distance of 0.19 m from the optical measurement location to the hot film location was found to be 0.235 ms. The beginnings of the turbulent spots in Figure 7 are marked by vertical dashed-dotted lines and the dotted lines are offset by this time delay, indicating when the turbulent spot should appear over the hot film sensor. In general, the agreement between the predicted and the actual beginning of the turbulent spot are good. In some cases, like in Figure 7, bottom left, the spot arrived to the hot film slightly faster, or, as in Figure 7, bottom right, slightly later, implying that the leading edge of the turbulent spot is not fully axisymmetric, with some portions of it advancing or retarding; however, this asymmetry appears to be small.

The leading edge in the hot film time series is easily identifiable; unfortunately the exact time of the trailing edge arrival cannot be defined using the hot film, so the convective speed of the trailing edge cannot be accurately computed. However, it turns out that the convective speed of the trailing edge can be measured using optical data only.

The wavefronts over the full aperture were measured during Run B2 and the spatial root-mean-squared of the wavefronts, denoted $OPD_{RMS}(T)$, were computed at different moments during the turbulent spots. Total of 31 turbulent-spot events were analyzed and the ensemble-averaged OPD_{RMS}, normalized by the time-averaged OPD_{RMS} of the fully turbulent boundary layer, are presented in Figure 8 as a function of the normalized time, zero corresponding to the leading edge of the turbulent spot and one corresponding to the trailing edge of the turbulent spot. Error bars denote standard deviations inside each ensemble. Optical distortions increase during the first 30% of the spot duration and reaching a normalized value of 0.65. After that, the normalized value of OPD_{RMS} starts decreasing, except for the sharp increase around the normalized time of 0.8, which will be discussed later. As OPD_{RMS} is proportional to the local boundary-layer thickness, it indicates that the turbulent spot reaches its maximum thickness of approximately 65% of the thickness of the fully turbulent boundary layer around the normalized time of 0.3 and monotonically decreases after that. Qualitatively, it agrees with the results of numerical simulations of the turbulent spot evolution at $M = 6$, although the simulations were performed at earlier stages of the turbulent spot evolution. On average, the thickness of the turbulent boundary layer is approximately twice thinner than the regular turbulent boundary layer.

The deflection angles over the aperture for Run B8 were spatially cross-correlated between the adjacent frames to compute the local convective speed, U_C, of the different moments during the turbulent spot. Ensemble-averaged results for 12 turbulent-spot events, normalized by the freestream speed, are shown in Figure 9 as a function of the normalized time during the turbulent-spot event. The convective speed is approximately $0.95U_\infty$ during the first 40% of the turbulent spot duration and starts decreasing after that, reaching values of approximately $0.92U_\infty$ by the end of the turbulent spot. The speed exhibits a sharp drop to $0.75U_\infty$ around the normalized time of 0.8, coinciding with the sudden increase in OPD_{RMS}-value, shown in Figure 8. Analysis of the convective speed results for all studied events have revealed that the time of the speed drop is correlated with the arrival of the trailing edge. Both the OPD_{RMS} increase and the convective speed drop occur 0.284 ms before the passage of the trailing edge of the turbulent spot (Figure 9 inset).

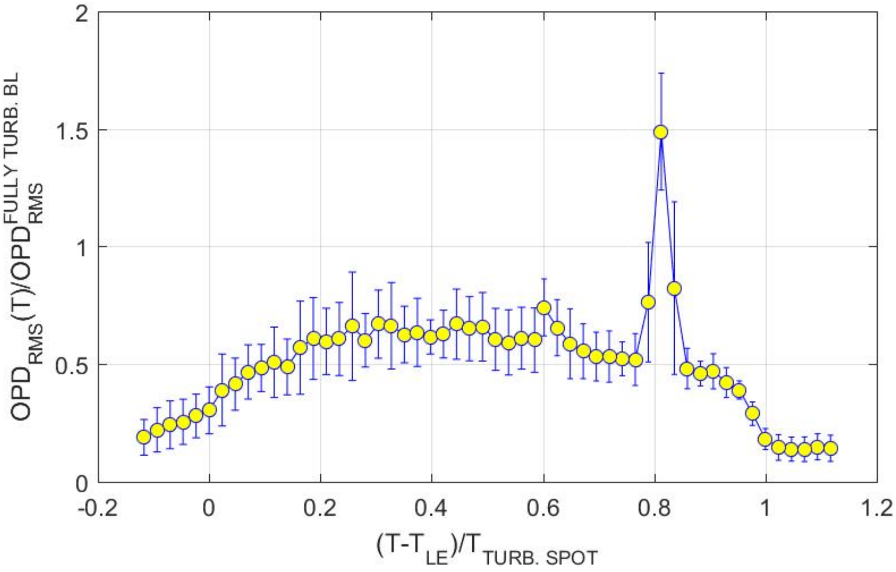

Figure 8. Ensemble-averaged $OPD_{RMS}(T)$, divided by time-averaged OPD_{RMS} for the fully turbulent boundary layer, as a function of the normalized time during the turbulent spot. Error bars denote standard deviations inside each ensemble.

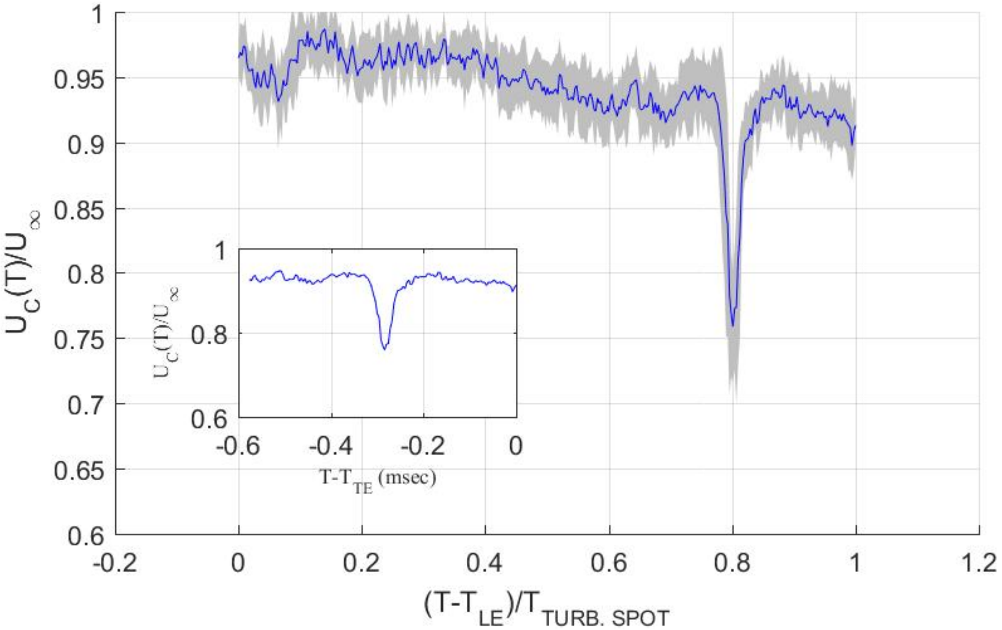

Figure 9. Ensemble-averaged convective speed, $U_C(T)$, normalized by the freestream speed, as a function of the normalized time during the turbulent spot. Gray region denote standard deviations inside each ensemble. The inset shows the normalized convective speed as a function of time, relative to the trailing edge arrival.

This anomalous behavior in the optical levels and the convective speeds can be explained by considering a turbulent spot moving within the axisymmetric tunnel. The turbulent spot is thicker than the surrounding laminar boundary, so the change in the displacement thickness between the laminar and the turbulent boundary layer will change the fluidic surface. If the relative difference between the moving leading or trailing edges and the freestream flow is larger than the speed of sound, a moving Mach wave will appear; these waves have been observed in shadowgraph pictures of turbulent spots on a cone [21]. As the turbulent spot was found to be approximately axisymmetric [4], the moving Mach wave is approximately conical, as schematically shown in Figure 10, left. The conical Mach wave is generated by the trailing edge, so it will also travel at the same convective speed as the trailing edge. At the tip of the cone, aero-optical distortions are the largest; when this region of the increased aero-optical distortions passes over the laser beam, overall aero-optical distortions will increase, as shown in Figure 8 around the normalized time of 0.8. The inspection of the full-aperture wavefront at the moment of the largest optical distortions had shown evidence of the wedge-type wavefront due to the tip of the conical Mach wave, see a representative wavefront in Figure 10, right.

Knowing the time delay between the arrival of the tip of the conical wave and the trailing edge to the measurement station, the tunnel diameter and the freestream speed, the convective speed of the conical wave and, consequently, the speed of the trailing edge can be computed. The angle of the moving conical wave, μ, is related to the relative speed between the freestream and the trailing edge speeds, $\sin(\mu) = \dfrac{a_\infty}{U_\infty - U_{TE}} = \dfrac{1}{M_\infty (1 - U_{TE} / U_\infty)}$. The distance between the trailing edge and the tip of the wave, L, is $L = R \tan(\mu)$, where $R = 0.1205$ m is the tunnel radius. Finally, the time delay is related to this distance as $T_{\text{delay}} = L / U_{TE} = 0.284$ ms. Solving all of these equations gives $U_{TE}/U_\infty = 0.706$ and $\mu = 34.6$ degrees. This value of the convective speed for the trailing edge generally agree with the value of $U_{TE}/U_\infty = 0.67$, obtained by analyzing the time traces of the unsteady wall pressures in this tunnel [4], as well as the value of $U_{TE}/U_\infty = 0.68$ obtained from numerical simulations for the turbulent spot at M = 6 [22].

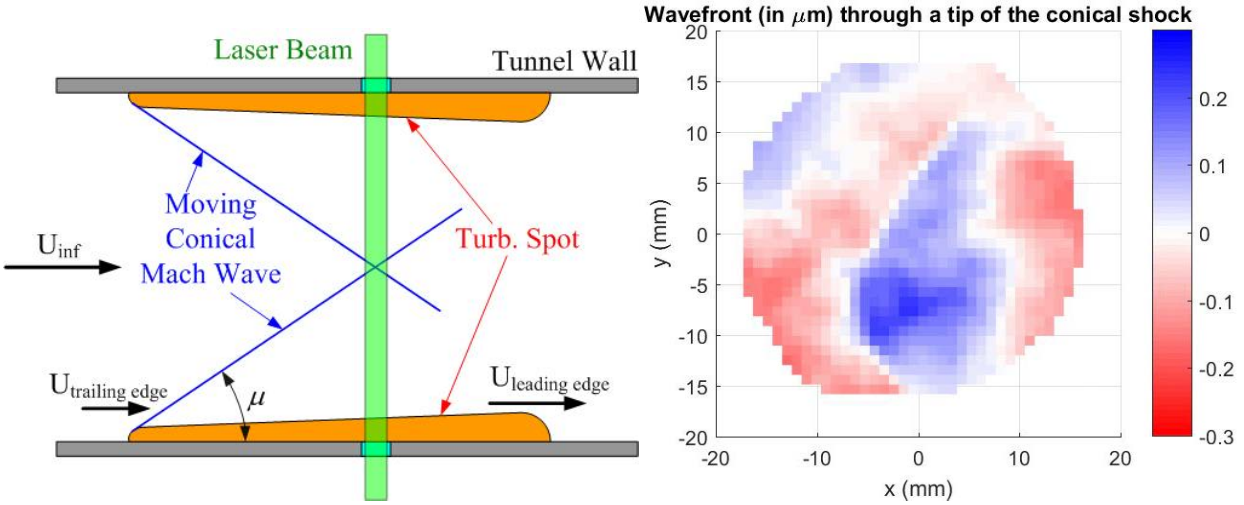

Figure 10. Left: Schematic of the moving axisymmetric turbulent spot and the attached conical Mach wave, generated by a mismatch between the displacement thicknesses. Right: A representative wavefront, corresponding to the increase in aero-optical distortions in Figure 8. A wedge-type structure, corresponding to the tip of the conical wave is clearly seen.

When the laser beam travels through both the faster-moving turbulent spot on the tunnel wall and the slower-moving tip of the conical shock in the middle of the tunnel, the wavefront represents the integrated value of the aero-optical distortions. As a consequence, the resulting measured convective speed should in between these convective speeds, which explains why the minimal optically-related speed in Figure 9 is only 0.76 of the freestream speed.

As a final remark, as the convective speed of the leading edge is about 0.95 of the freestream speed, the relative speed is subsonic and, therefore, the leading edge does not generate the Mach wave.

Knowing that the front and the leading and the trailing edges of the turbulent stop move at different speeds of 0.95 and 0.71 of the freestream speed, correspondingly, traveling times from the nozzle throat throughout the tunnel to the measurement station can be calculated and presented in Figure 11. At the measurement station the difference between two arrival times was found to be approximately 1 ms. It corresponds to the lower bound of time duration of the turbulent spot, as the turbulent spot moves at slower relative speeds of 0.9 for the leading edge and 0.6 for the trailing edge at smaller Reynolds numbers (or, equivalently, closer to the nozzle throat). Using these relative values of the convective speeds gives the upper bound of the turbulent-spot duration of 1.4 ms. These estimated values of the turbulent spot duration are very close to the experimentally-observed ones in Figure 5, further indicating that the turbulent spot originates in the tunnel nozzle and eventually engulfs the whole tunnel wall by the time it reaches the measurement station 1.9 meters downstream of the nozzle throat.

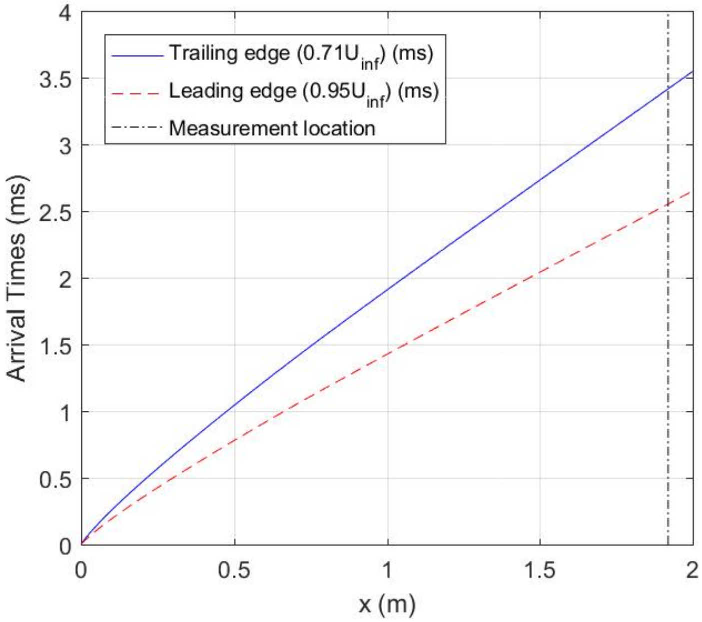

Figure 11. Traveling times for the leading and the trailing edges of the turbulent spot along the test section.

Transitional second mode

Another transitional event, observed in the laminar boundary layer at high Reynolds numbers is shown in Figure 4, bottom right, with additional deflection-angle time traces shown in Figure 12. These events correspond to a wave-packet single-frequency signal, fundamentally different than the turbulent spots discussed previously. Analysis of the time series has shown that the duration of the single mode is typically between 0.1 and 0.2 ms or 12-25 δ/U_∞. Occasionally, several events appear to combine, resulted in a longer time series, see the most top time series in Figure 12, for example. So, these events are more-localized events, compared to order-of-magnitude larger turbulent spots.

Deflection-angle spectra, computed for several of these events, are shown in Figure 13, along with the laminar boundary layer spectrum for comparison. These single-mode events were found have a range of frequencies between 65 and 80 kHz, corresponding to a second transitional mode with the frequency of $0.5U_\infty/\delta \sim 70$ kHz [4,18], indicated as a dashed line in Figure 13.

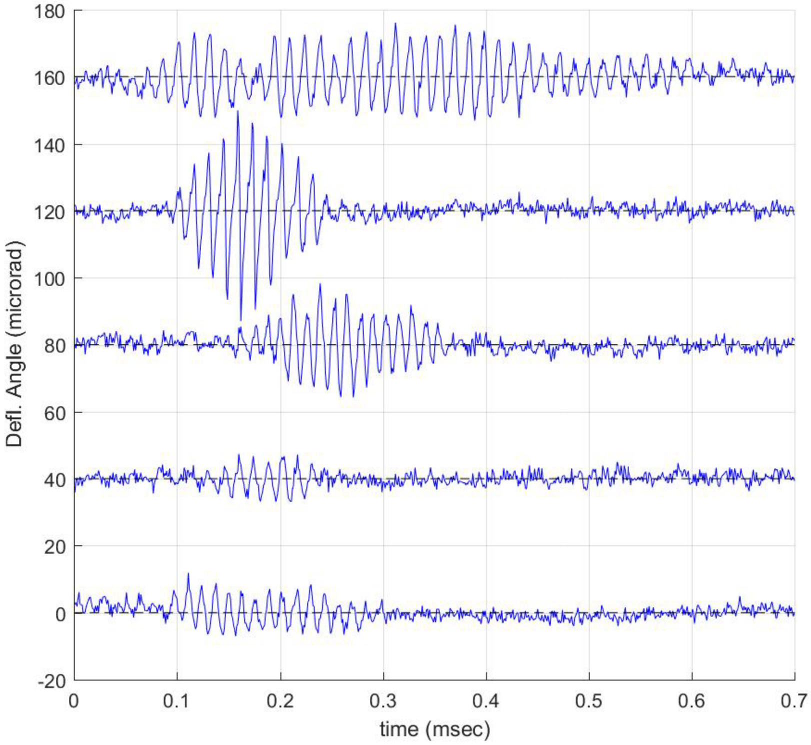

Figure 12. Examples of deflection-angle time series with a transitional single mode present. Each successive time series is vertically offset by 40 microradians.

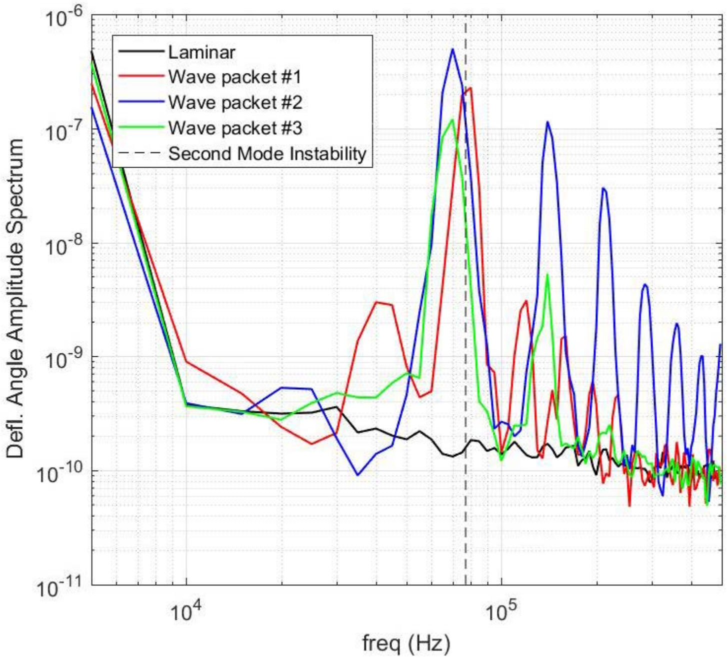

Figure 13. Deflection angle spectra of the laminar boundary layer and for several single mode events. Theoretical prediction of the second-mode instability is given as a vertical dashed line.

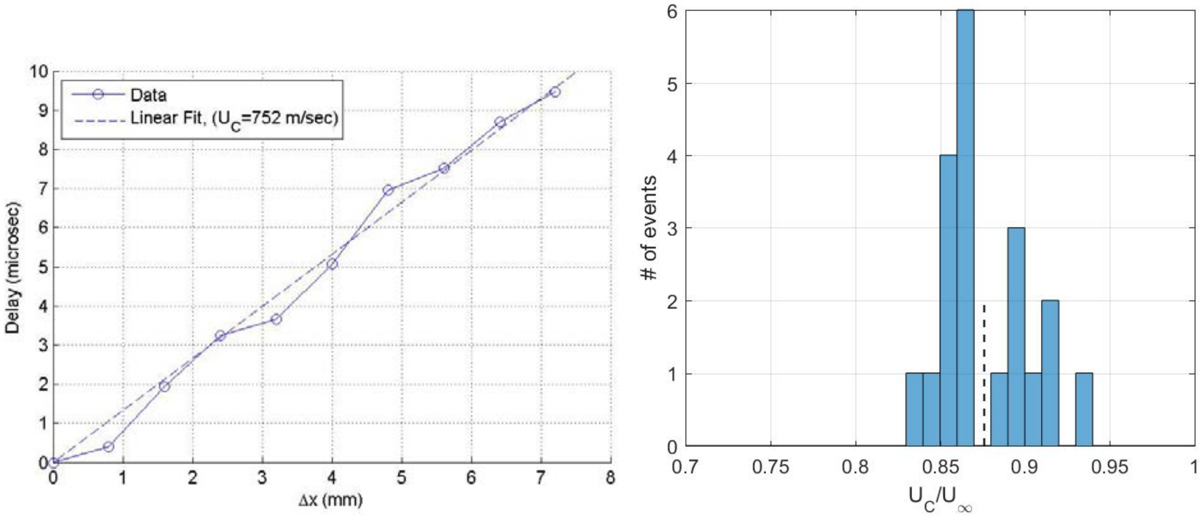

Figure 14. Left: calculations of the convective speed using time-delayed correlation method.

Runs A8, A11, B4 and B6 were used to compute the convective speed of the second-mode events, using the correlation-based method, outlined before. An example of the delay dependence on the separation between spatial points over the aperture is shown in Figure 14, left. A linear fit through the points gives a corresponding convective speed of 752 m/s. Analysis of 20 second-mode events, with the distribution shown in Figure 14, right, allows estimating the convective speed to be $U_C = 760 \pm 23$ m/s or $U_C/U_\infty = 0.88 \pm 0.03$. Using this convective speed, the averaged wavelength of the second mode was found to 10.4 mm or 1.86δ.

Knowing the spatial wavelength of the second mode, a conditional search of all wavefront spatial-temporal sequences, corresponding to this spatial wavelength, was performed for Run A2, where the wavefronts were sampled with the largest, ~6δ, spatial resolution. When the event was detected over the aperture for several sequential frames, a frozen field hypothesis was used to "stitch" the wavefronts into pseudo-spatial "snapshot" of the second-mode structure. Several examples of the spatially-reconstructed second-mode structures are shown in Figure 15. Note that the overall amount of aero-optical distortions during these events is fairly small, between -0.03 and 0.03 microns; nevertheless, the optical set-up was sensitive enough to detect these structures. No controlled disturbances were introduced into the boundary layer --- these are naturally occurring wave packets. All these extracted structures show the presence of a streamwise-periodic pattern with the spanwise size of approximately $2\text{-}3\delta$ and extended between 30δ and 60δ in the streamwise direction.

In some cases, like the top two examples in Figure 15, the structure is not significantly distorted in the spanwise direction, while in other cases, presented in the bottom four examples, the structure shows the presence of the oblique structure edges, or "wings", on both spanwise sides of the structure. These "wings" exhibit an unusual "reverse-bow" behavior, as they lead the main body of the structure (the 'head"). It contradicts the results of the second-mode studies, performed in this tunnel, using the series of streamwise/spanwise-arranged unsteady pressure sensors [4], where is was found that the "head" of the second-mode structure lead the "wings" in bow-like fashion. The exact reasons of this discrepancy is currently under investigation, however let us make a couple of points. In [4] all measurements were performed at lower stagnation pressures below 150 psi. As the second-mode structures do not appear naturally under these conditions, the second-more structures were created by periodic pulsed-glow perturbations, imposed on the tunnel wall upstream of the measurement station. Knowing the exact location and frequency of the perturbations, they used conditional averaging to reconstruct the wall pressure "footprint" of the structure at different distances downstream of the source of the perturbations. In our case, the second-mode structure naturally and randomly occurred in the flow. Each stitched wavefront sequence is an individual event; there is no ensemble averaging of wave packets in the wavefront sensor data. Furthermore, we were looking for a particular spatial pattern to extract the structures, so it is possible that we found only a particular sub-set of the structures, which satisfied this search pattern. Finally, the numerical simulations on the transitional second-mode structures, performed on a cone at Mach 6, [23] also showed that the "wings" of the transitional structure are ahead of the structure "head", qualitatively similar to what was observed in Figure 15.

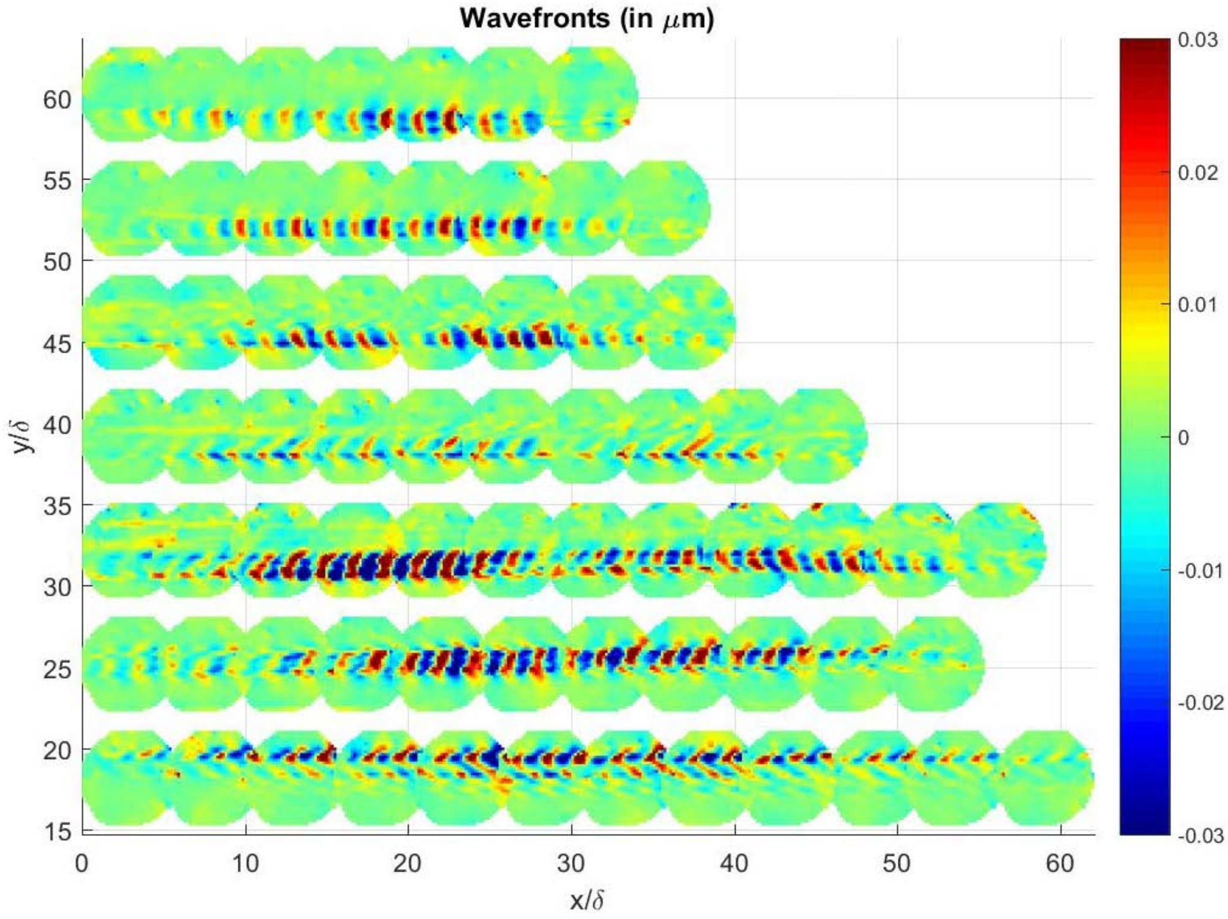

Figure 15. Examples of "stitched" 2-D wavefronts corresponding to the second-mode transitional structures. Wavefronts are vertically offset for clarity. Flow goes from left to right.

V. Conclusions

Direct measurements of aero-optical disturbances imposed by naturally occurring transitional structures in the hypersonic laminar boundary layer at M = 6.0 were performed in the Boeing/AFOSR Mach-6 Quiet Tunnel at Purdue University. These transitional structures were observed only at high stagnation pressures above 150 psi, corresponding to Reynolds numbers greater than 11.5 M/m. Two types of transitional structures were non-intrusively studied: turbulent spots or bursts and second-mode instability waves. For turbulent spots, analysis of the aero-optical data gave a statistical distribution of the spot durations; the mean value was found to about 1.4 ms, placing the origin of the turbulent spot in the nozzle throat. The spots engulfed the full test section at the measurement location, with both the leading and the trailing edges been approximately axisymmetric. The ensemble-averaged aero-optical spectrum had revealed that the boundary layer inside the turbulent spot resembles the fully turbulent boundary layer. Detailed measurements of aero-optical distortions during the turbulent spot event showed that the boundary layer is about 50% of the thickness of the fully turbulent boundary layer, is the thickest in the beginning of the spot and decreases toward its end. By performing cross-correlations between wavefronts, the convective speeds inside the spot were also determined; it had a largest speed of 0.95-0.97 U_∞ in the beginning of the spot, with a gradual decrease to 0.92 of U_∞ by the end of it.

The optical distortions created by a conical Mach wave, generated by the moving trailing edge of the turbulent spot, were observed. Based on the direct measurements of the location of the conical-shock tip, relative to the trailing edge, the convective speed of the trailing edge of the turbulent spot was found to be 0.7 U_∞.

The second type of the observed transitional structures were the second-mode instability wave packets or structures. It is characterized by a predominantly-single frequency of 65-80 kHz, and found to be in agreement with the theoretically-predicted frequency of 0.5 U_∞/δ. The convective speeds were directly measured by cross-correlating aero-optical distortions, with the mean speed of 0.88 U_∞. In order to study the streamwise/spanwise topology of the structures, sequential wavefronts were “stitched” together, using the frozen field assumption. The structures were found to be fairly narrow, about 2-3δ in the spanwise direction, while extending for 30-60δ in the streamwise direction. An unusual “reverse-bow” pattern was observed on most of them, when the “wings” of the structure were found to advance relative to the main structure body.

Overall, direct non-intrusive aero-optical measurements were found to provide very useful information about the transitional structures in the hypersonic laminar boundary layer. We believe it was the first time aero-optical environment, relative to these transitional structures, was experimentally studied. Combined with other instruments, it gives important complimentary information about the spatial-temporal evolution of the density field inside these structures.

Acknowledgements

The authors would like to thank Prof. Steven Schneider of Purdue University for the opportunity to use the BAM6QT to perform these measurements. Also we would like to express our gratitude to Brandon Chynoweth for his help preparing the experiment.

References

[1] Jumper, E.J. and Fitzgerald, E.J., 2001, “Recent Advances in Aero-Optics,” *Progress in Aerospace Sciences*, **37**, 299-339.

[2] Wang, M., Mani, A. and Gordeyev, S., “Physics and Computation of Aero-Optics”, *Annual Review of Fluid Mechanics*, **44**, pp. 299-321, 2012.

[3] S.P. Schneider, "Laminar-Turbulent Transition on Reentry Capsules and Planetary Probes", *J. of Spacecraft and Rockets*, **43**(*6*), pp. 1153-1173, 2006.

[4] K.M. Casper, S.J. Beresh and S.P Schneider, “Pressure fluctuations beneath instability wavepackets and turbulent spots in a hypersonic boundary layer,” *J. Fluid Mech.* **756**, pp. 1058-1091, 2014.

[5] T.J. Juliano, "Nozzle Modifications for High-Reynolds-Number Quiet Flow in the Boeing/AFOSR Mach-6 Quiet Tunnel", PhD. Thesis, Purdue University, 2006.

[6] K. M. Casper, “Hypersonic Wind-Tunnel Measurements of Boundary-Layer Pressure Fluctuations”, M.S. Thesis, Purdue University, 2009.

[7] S.P. Schneider, "Effects of Roughness on Hypersonic Boundary-Layer Transition", *Journal of Spacecraft and Rockets*, **45**(*2*), pp. 193-209, 2008.

[8] Gordeyev, S., Smith, A.E., Cress, J.A. and Jumper, E.J. “Experimental studies of aero-optical properties of subsonic turbulent boundary layers,” *Journal of Fluid Mechanics*, **740**, pp. 214-253, 2014.

[9] Gordeyev, S., Jumper, E.J. and Hayden, T., "Aero-Optics of Supersonic Boundary Layers," *AIAA Journal*, **50**(*3*), 682-690, 2012.

[10] Wyckham, C. and Smits, A. “Aero-Optic Distortion in Transonic and Hypersonic Turbulent Boundary Layers,” *AIAA Journal*, **47**(*9*), pp. 2158-2168, 2009.

[11] A.E. Smith, S. Gordeyev, H. Ahmed, A. Ahmed, D.J. Wittich III and M. Paul, “ Shack-Hartmann Wavefront Measurements of Supersonic Turbulent Boundary Layers in the TGF,” AIAA Paper 2014-2493.

[12] E. Tromeur, E. Garnier and P. Sagaut, “Large-eddy simulation of aero-optical effects in a spatially developing turbulent boundary layer”, *Journal of Turbulence*, **7**, 2006.

[13] E. Tromeur, P. Sagaut and E. Garnier, “Analysis of the Sutton Model for Aero-Optical Properties of Compressible Boundary Layers “ *J. Fluids Eng.* **128**(*2*), 239-246, 2005.

[14] White, M. and Visbal, M., “Simulation of Aero-Optical Interactions in Transonic Boundary Layers," AIAA Paper 2011-3279, 2011.

[15] T. J. Juliano, S. P. Schneider, S. Aradag and D. Knight, "Quiet-Flow Ludwieg Tube for Hypersonic Transition Research", *AIAA Journal*, **46**(*7*), pp. 1757—1763, 2008.

[16] B. M. Wheaton and S. P. Schneider, "Roughness-Induced Instability in a Hypersonic Laminar Boundary Layer", *AIAA Journal*, **50**(*6*), pp. 1245—1256, 2012.

[17] A. Chou, "Mach-6 Receptivity Measurements of Laser-Generated Perturbations on a Flared Cone", PhD. Thesis, Purdue University, 2014.

[18] B. M. Wheaton, "Roughness-Induced Instabilities in a Mach-6 Laminar Boundary Layer", PhD. Thesis, Purdue University, 2012.

[19] Southwell, W. H., “Wave-front estimation from wave-front slope measurements,” Journal of the Optical Society of America, **70**(*8*), pp. 998-1006, 1980.

[20] S. Gordeyev and T.J. Juliano, “Optical Characterization of Nozzle-Wall Mach-6 Boundary Layers,” AIAA Paper 2016-1586, 2016.

[21] S.P. Schneider, “Hypersonic laminar-turbulent transition on circular cones and scramjet forebodies,“ *Progress in Aerospace Sciences*, **40**(*1*), pp. 1–50, February 2004.

[22] Krishnan, L. and Sandham, N. D., “Effect of Mach Number on the Structure of Turbulent Spots,” *Journal of Fluid Mechanics*, **566**, pp. 225–234, 2006.

[23] J. Sivasubramanian and H.F. Fasel, Numerical Investigation of Laminar-Turbulent Transition in a Cone Boundary Layer at Mach 6,“ AIAA Paper 2011-3562, 2011.